Observational Study of Clogging Specimens from the Tundish Well Showing Origin and Growth of a Clog in an Al-Killed Ti-Alloyed Steel Cast

BERNADETA KARNASIEWICZ and ENNO ZINNGREBE

Post-mortem tundish skull samples of Ti-alloyed, Al-killed IF steel have been studied regarding the formation of clogging. By using modern characterization equipment and applied methods, we performed a detailed characterization of microstructures found in the tundish well. Aside from the primary metallographic examination, newly developed methods of particle size distribution analysis based on population density functions (PDF) and newly developed electron microscope EDS template mapping have been applied, allowing differentiation of complex particles according to phases and interphase contact relationships. Furthermore, detailed EDS analyses of individual inclusions with complex substructure regarding minor and trace elements within the alumina networks have been performed. These composite data on carefully selected clog microstructures allowed us to observe the presence of layering microstructures throughout the clog: "Coarse" layers (abundant microbubbles and internally complex alumina aggregates) and "Fine" layers (no microbubbles and complex alumina aggregates). Two populations of particles: Population I (2 to 5 μm) and a Population II (5 to 20 μm) build up the layers, both having lognormal PDF, in contrast to power-law PDF of secondary metallurgy inclusions. Coarse layers are further distinguished by selective concentrations of spinel with lognormal PDF as well as the occurrence of complex alumina particles with metal sub-inclusions often with elevated Cr, V, and Si content. Based on these observations, we derive a model for the origin and accumulation of the inclusions making up the clog, which suggests that the NMI of the two dominant populations do not come from the bulk steel, although secondary metallurgy-derived inclusions can be traced in the clog. Overall, microstructures show that the clog behaves as a coherent solid, and is able to displace and fracture.

I. INTRODUCTION

IN the production of Al-killed steel grades, non-metallic inclusions (overwhelmingly alumina Al_2O_3) cause the impediment and ultimately blockage of flow in critical places of the casting installation, which is ubiquitously known as clogging phenomenon. While research on causes and countermeasures to clogging is ongoing since over 40 years,[1–5] still very little is known about the actual formation and aggregation processes of clogging deposits from observations in the industrial practice.[6–8] Most current research on the formation of clogging deposits assumes the operation of certain physical processes and explores their development over time using various types of modeling.[9–13] Overall, the suggested mechanisms for the clogging origin fall into two conflicting hypotheses:

1. attachment of particles existing in the steel bath to the refractory or to pre-existing clogging deposit at the location of the clogging growth (depositional models[2,10,12–15]);
2. formation of new *in situ* particles at the location of the clogging deposit, due to chemical reactions such as reoxidation (sidewall reaction models[4,5,16–19]);

both eventually causing the termination of liquid steel casting.

Clogging by alumina particles is known to occur in two main structural types:

– in the form of alumina powder along refractories and in powder-filled voids (gas bubbles[2,4,20,21]), most often in the Submerged Entry Nozzles;
– as alumina grain aggregations within the steel matrix, which is often encountered in ladle or tundish nozzles

BERNADETA KARNASIEWICZ is with the Niebylec, Poland and also with Tata Steel, R&D, P.O. Box 10,000, 1970 CA IJmuiden, The Netherlands ENNO ZINNGREBE is with Tata Steel, R&D. Contact e-mail: Enno.Zinngrebe@tatasteeleurope.com

and other surfaces of the casting installations, especially in the casting of Ti-alloyed steels.[1,2,7,14,16,22]

While the contrast between these two forms of clogging deposits is well known in the industrial practice, the reasons for their respective occurrence and distribution in conventional casting systems are not well understood. For loose or only slightly sintered powder of alumina grains as often observed in SENs, reference is often made to the non-wetting character of the steel-to-alumina contact leading to phase separation of inclusions from liquid metal especially as argon is added as anti-clogging countermeasure through porous nozzles. Yet, in the same casts, fully metal-penetrated, aggregated alumina networks are found covering the nozzles at which argon is injected. Given this continuing lack of clarity on the microphysics underlying this difference, there have been renewed efforts to study the microstructures and formation of clogging deposits from metallographic specimens either of experimental samples[7] or of post-mortem samples directly from the industrial process,[16,23] making use of the improved capabilities of modern characterization tools compared to the early research. Specifically, the formation of the fully metal-infiltrated clogging deposits needs improved understanding, as it is rich in detailed microstructures[1,2,7,14,15,23] that have not yet been adequately explained in terms of a formation mechanism. In this study, we want to contribute a new observational dataset on the microstructures of these deposits, which supports in our interpretation a very specific proposal for the mechanism of the buildup of tundish clogging deposits and for the origin of the non-metallic inclusions (NMI) encountered in it.

A. *The Samples*

The steel is cast through a conventional caster, from the ladle through a slide-gate regulated ladle shroud into a 70-ton capacity tundish, feeding two casting strands equipped with slide-gate-regulated tundish nozzles. For the composition of the cast described here, see Table I. From the industrial experience, it is known that this steel tends to clog by the formation of clogging deposits in the tundish nozzle, upstream of the regulating slide gates. In order to sample a residual steel after casting, an ordinary 10-heat cast series was terminated by leaving approximately 7 tons of the steel in the tundish. For the investigation of clogging phenomena, the steel skull has been sampled at various locations. This study is focused on the sampled steel skull filling the upper tundish nozzle (Figure 1), which is known as a critical location of clogging growth. The nozzle has an inner bore width of 8 cm and is surrounded by a high-alumina porous nozzle stone through which Ar is injected during cast as a clogging countermeasure. The nozzle skull was cut through and etched with Nital (5 pct) for visual inspection, showing the occurrence of up to 2.8-cm-wide

Table I.   Typical Composition of the Ti-Alloyed Al-Killed Steel Casts

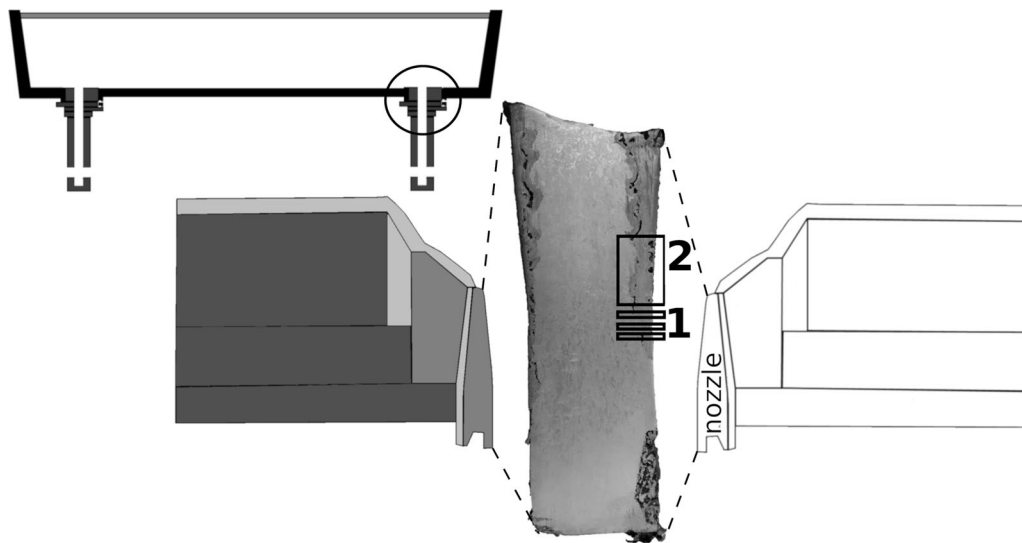| Element	C	N	S	Al	Si	Ti	Mn
Ppm	15 to 20	20	70	200 to 400	30 to 50	400 to 500	1100

Fig.1—A sketch of the tundish well combined with an image of the etched nozzle cross-section of the obtained skull, showing the details of clogging deposit along the nozzle (darker gray areas). The nozzle orifice is 8 cm wide and the widest clogging thickness is 2.8 cm (upper right corner). Numbers 1 and 2 indicate the locations of the samples taken for the present study (a vertical section along-flow and three horizontal sections across-flow).

clogging deposits along the margins of the nozzle. A sketch of the tundish well, together with an image of the etched tundish nozzle cross-section is shown in Figure 1.

Figure 1 shows the clogging deposit recognizable as darker gray etched areas along the sides of the skull. The deposit shows both of the above-mentioned forms of clogging: large voids (bubbles) filled with loose alumina grain powder, which appear black, and areas of metal containing large numbers of NMI that form an interconnected network, giving the skull a dark gray appearance after etching (detailed microscopic images of both types of deposit are shown below). The general morphology of the clog is similar to that described in Reference 23 for this type of steel: the deposition narrows down into the vertical part of the nozzle. In detail, the clogging deposit is irregular in surface and contains large powder-filled bubbles which appear to align as if marking a specific transient surface. Additionally, irregular mixes of powder-filled voids and steel containing NMI appear at the lower end of the nozzle cross-section (Figure 1).

To investigate the clogging deposit in detail, sample locations along the nozzle cross-section surface were selected (Figure 1). While 16 samples along the overall tundish skull were taken and analyzed in detail,[24] this study concentrates on the most informative local microstructures, shown by the two selected sample locations (Figure 1). Three horizontal sections (1A, 1B, 1C from top to bottom) through the deposit were made to analyze the appearance of the microstructure, and to trace the 3D morphological shape of the clogging deposit from the adjoining section cuts. The sections were made with approximately 5 mm vertical distance. Directly above, another sample was cut vertically (parallel to the flow), where most of the various microstructures could be observed (sample 2). All the samples were prepared for metallographic observation with 0.25 μm diamond finishing paste.

B. Methods

Standard reflected light optical examination has been performed on polished samples, using Zeiss Axioplan manual and Zeiss Z1 Imager automated microscopes equipped with Zeiss AxioVision 4.8 software. Automated image mappings in plane-polarized reflected light, at magnifications from $\times 50$ to $\times 500$, have been used to document the microstructures. Optical particle analysis of clogging deposits has been conducted using the image analysis functions—thresholding, segmentation, and object measurement—in AxioVision 4.8 software. Electron imaging and microchemical analysis has been done on a Jeol 7100F FEG SEM. Standard observations were made under 15 kV acceleration voltage but depending on the material supplemental observations were made with accelerations ranging from 0.5 to 10 kV. Samples were generally observed in BSE contrast mode showing the chemistry (mean Z) as image contrast. Probe currents ranged from 1 to 4 nA, depending on conditions, and samples were mostly carbon coated against charging. Horizontal spread of the excitation volume under standard operation conditions was 1 to 1.5 μm.

Chemical analyses were performed by EDS with standardless ZAF correction using the Thermo Noran System Six and Pathfinder analytical software. Standard analytical counting time was 15 seconds, but prolonged counting times up to 300 seconds were used for better minor element detection. Automated Inclusion Analysis (AIA) by SEM has been performed on the selected areas of clogging deposits using Feature Sizing functions of the Pathfinder analytical software. Particle population data obtained by light-optical or electron-optical image analysis, which are two-dimensional cross-section data, were recalculated into modeled underlying three-dimensional particle population data using the stereological applet CSDCorrections (v. 1.40) obtainable at http://www.uqac.ca/mhiggins/csdcorrections.html,[25,26] generally following procedures outlined in References 23, 27, and 28. The stereology conversion assumes that each particle cross-section seen in an image is the cross-section of an individual particle, albeit not necessarily a central section. For isolated particles in liquid steel, this tends to be true. In the clogging deposits, the particle volume fraction can exceed 10 vol pct, and the interparticle distances can be micrometers only, therefore, it is well possible that complex-shaped clusters or dendrites of particles intersect the observed section plane multiple times, creating multiple independent 2D sections instead of the single particle. Conversely, it can be observed that many "objects" that are treated as a single section in image analysis, represent several originally distinct grains in more or less advanced stage of sintering. These effects are ignored in the applied stereology applet, creating a systematic error in the apparent PDFs found compared to actual 3D PDFs in the clogging deposit. However, the direction of this offset is known, as the coagulation and sintering of particles is precisely the process that turns an original lognormal size-distributed population of particles into a power-law distributed one in the steel ladles (see discussion in the results section). The effect of this misrepresentation is to make the apparent observed PDF more linear looking than the underlying real PDF.[29] That this effect operates in this way has been tested by experiments with manual separation of particles on selected images before image analysis, confirming that the sintering effect acts to linearize apparent sectional PDFs (not shown in this study).

II. RESULTS

A. Horizontal Sample Set 1A, 1B, 1C

The successive microstructures of three horizontal samples indicated in Figure 1 are shown in Figure 2 as a set of 3 reflected light overview images. Along the direction of the flow, the top sample is image 1A, middle 1B, and the last one is 1C. The set of microstructures in Figure 2 represents a continuum of dynamically changing clogging deposit morphology along the nozzle bore. The contact between deposits and edge of the nozzle wall is indicated by the dashed line in Figure 2(1C). A large pocket of loose alumina powder roughly follows
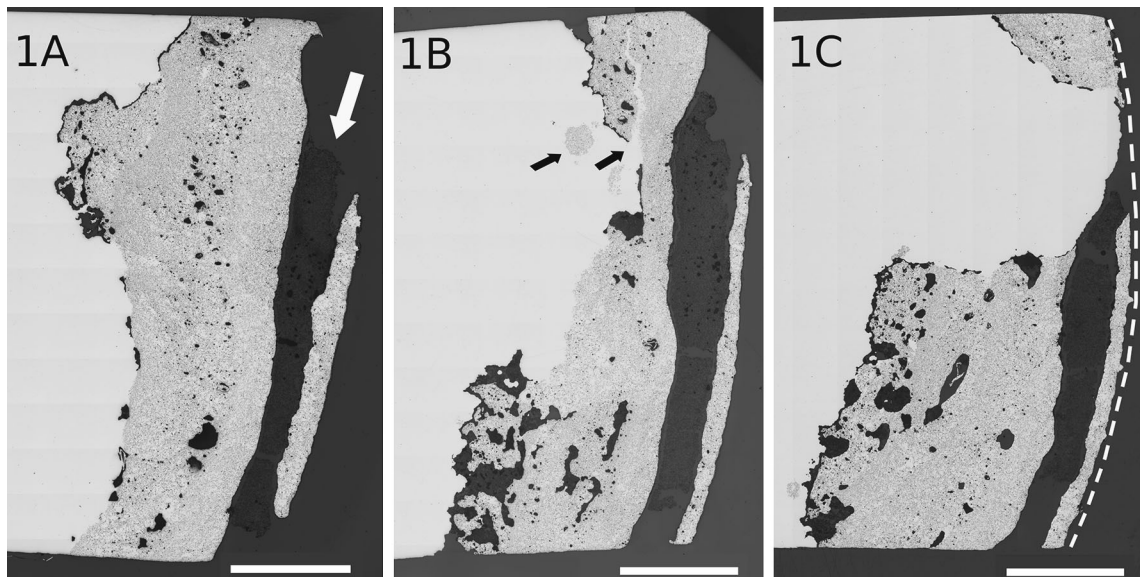
Fig.2—A set of overview images of the samples taken horizontally from the tundish nozzle, where the sections 1A, 1B, and 1C represent the cuts along the sidewall from the location indicated in Fig. 1. The scale bars have a length of 5 mm. The white dashed line in section 1C indicates the location of the nozzle bore edge. White arrow in image 1A points out the pocket of loose alumina powder. Black arrows in image 1B indicate remnant crack in clogging deposit as well as unconnected round alumina cluster (see discussion in the text).

the sidewall (white arrow in 1A), and the main mass of the clogging deposit rests on this powder pocket, not on the original refractory contact. A thin sheet of steel full of Al_2O_3 inclusions lies along the original edge of the nozzle. The main clogging deposit itself has a noticeable content of voids (either empty or filled with alumina powder). Further, the inner surface of the clogging deposit to the free steel has an irregular shape, which is particularly visible in section 1B. A remnant of a crack in a surrounding of dense clogging deposit is visible in section 1B (black arrow), just above a large segment of missing clogging deposit (cf. 1C). Rounded alumina complexes appear disconnected from the main deposit in 1B (black arrow), but must be three-dimensionally connected with the clogging complex seen in 1A, since they would have been transported away by the steel flow, if disconnected. The remnant crack in sample 1B shows that the clogging deposit behaves as a solid. Thus, the alumina particles must be sintered together, forming a coherent network of aggregated inclusions, which therefore must be seen as a solid 3D structure. Our further interpretation of these microstructures is that there was a partial and sharp breakup of clogging deposit (1A to 1C). Roughly 12.5 mm of clogging material has been taken away by the stream of a liquid steel over a distance of ~ 2 cm along the tundish nozzle.

1. Summary

The clogging deposit is an accumulation of inclusions where the individual Al_2O_3 particles are strongly sintered together forming a 3D structure. The clog therefore can behave like a solid, even when subjected to such a dynamic steel flow in a tundish outlet. Moreover, at unknown time during casting, the clog can fracture and potentially feed large fragments back into the cast steel flow.

B. Sample 2: Parallel to the Tundish Nozzle Steel Flow

Sample 2 from the tundish nozzle seen in Figure 1 was cut along the flow direction. A reflected light optical full-sample overview image is shown in Figure 3. The inclusions embedded in the steel matrix are not homogeneously distributed but show a characteristic inner structural variety. The overall clogging deposit is ~ 9 to 13 mm thick, but it is interrupted by conspicuous areas of inclusion-free steel, as well as large voids (bubbles). Many of these microstructures have been seen already in the earliest descriptions of such clogging deposits,[1,2,15] also in the recent analysis of Reference 23 yet have not found systematic attention. Thus, the following subchapters focus on the details of the most informative clogging structures regarding the question of origin and formation of given networks. Areas of interest are marked with black outlines on Figure 3 as region 1 and 2.

1. Region 1: the layering

A magnification of region 1 of sample 2 (Figure 4) shows the alumina heterogeneity within this location. The inclusions in this region have formed a very explicit microstructure of regularly alternating layers. Such layering was not only observed in Figures 2, 3 and 4 but also in other samples across the tundish skull. As this phenomenon is barely described in the present literature, yet has direct implications for the formation of the clogging deposit as a whole, it is characterized here in detail:

– the first type of layers contains coarse inclusions accompanied with small microbubbles, (in brief we will call it "Coarse layer");
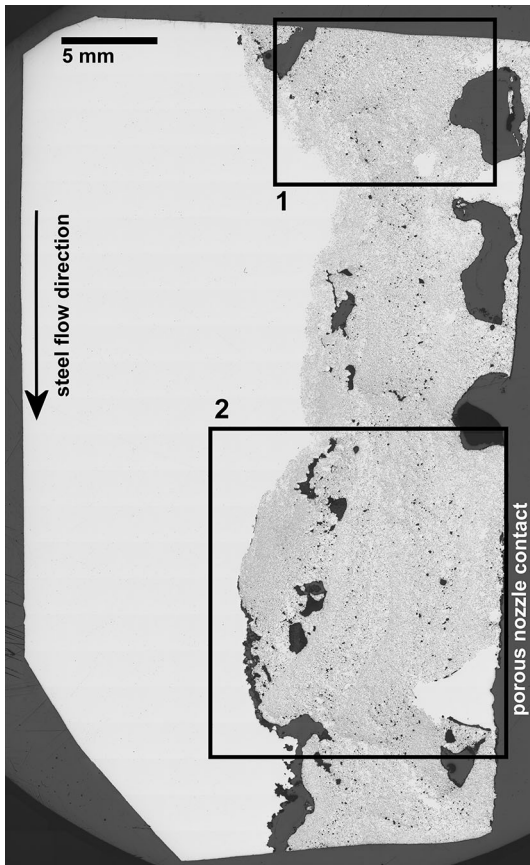
Fig. 3—Full-sample reflected light overview image of sample 2. Contact to the porous nozzle stone at right side, inner nozzle (free steel) at left side. Flow direction (down towards the sliding gate) and the region of interests are indicated with an arrow and squares 1 and 2, respectively.

– the second type of layers contains fine, densely packed inclusions and generally no microbubbles (in brief we will call it "Fine layer").

There is an additional layer of relatively fine-grained alumina particles running along the inner surface of the described layering region, which discordantly cuts across the layering structure (black arrows on Figure 4). This part of the deposit must therefore have been deposited later than the layered complex, and in brief we will call it "Overgrowth layer." From the observation of this whole microstructure it can be concluded that formation of this part of clog was clearly consecutive during the process.

In order to quantify and compare the inclusions of Coarse and Fine layers in this region, we performed particle size distribution analyses on the fine-scale microstructure shown in Figure 4. The layered complex has been divided into 7 distinguishable layers, according to their morphological characteristics (Figure 4): Layers no. 2, 4, and 6 are Fine layers, whereas layers no. 1, 3, 5, and 7 are Coarse layers. Particle sizes have been measured directly from the optical images (see Methods) at original magnification as seen in Figure 4 (insets). Two areas from layers 2 and 4 were taken as
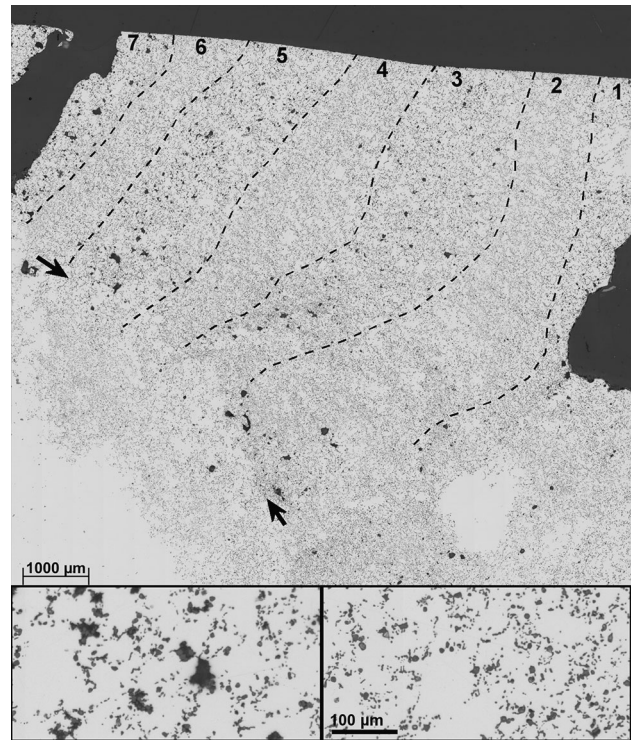

Fig. 4—The layering structure of clogging deposit of region 1 in Fig. 3, introducing the Coarse and the Fine layers. The layers are outlined by dashed lines, and are numbered at the top of the image. Exemplary microstructures at full resolution (×200 magnification) are shown by small images below: left image represents the Coarse layer and right image the Fine layer. An "Overgrowth layer" is indicated by black arrows.

representatives for the Fine layers, and two areas of layers 3 and 5 for the Coarse layers. Additionally, an area of the Overgrowth layer was taken for comparison.

The measurement data are summarized in Table II.

The optically observed cross-sectional data have been converted into population density functions (PDFs) (Figure 5). Population density functions have been used recently in analysis of NMI in steel as their properties are directly controlled by the chemical and physical processes shaping the particle populations. Previous work on NMI distributions in liquid Al-killed steel has shown that there are two different types of size distributions frequently occurring, that are linked to two different physical processes governing their development.[27,30] The formation of new alumina particles in steel, as happens during deoxidation, involves net material transfer from the solution (steel) to the growing particulate matter. Such net transfer growth leads to lognormal size distributions, in which the logs of particle sizes are normally distributed. Such lognormal size distributions are recognizable on a double-log PDF diagram (such as Figure 5) by their hump-shaped, inverted parabolic form. In contrast, in a steel in chemical equilibrium, the competition between physical forces clustering alumina particles together (interfacial tension/non-wetting behavior) and forces tending to break clusters up (microturbulence of the steel) creates a power-law size distribution, which is recognized on

Table II. Basic Observational Data for the Optical Particle Size Measurements (Figure 5)

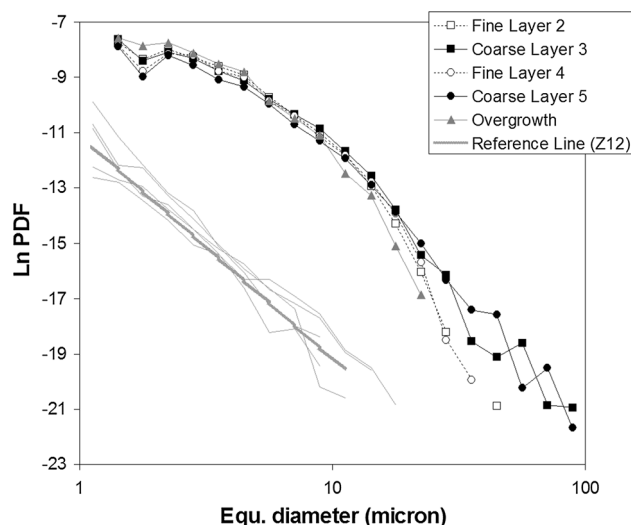|	Layer 2 Fine	Layer 4 Fine	Layer 3 Coarse	Layer 5 Coarse	Overgrowth Layer
Observed Area mm^2	3.6	2.2	1.9	1.7	0.75
N (Particles)	15,830	8920	8356	5545	3459
Av. Equ. Diameter μm	4.7	4.9	5.3	5.6	4.1
N/mm^2	4449	4124	4353	3342	4579

Fig. 5—Particle size distributions of alumina particles based on the optical segmentation in region 1 (from Fig. 3) in sample 2, with the distinction for two Coarse (filled symbols), Fine (open symbols) and the Overgrowth layer (gray triangles). For comparison, the PDF of alumina NMI in the same steel during steelmaking are also plotted as gray lines (from Ref. [28], a selected exemplary heat). The heavy gray line is the "reference line" for floating alumina, as defined by Ref. [28]; light gray lines give an indication of the scatter of data in a single heat (ladle and tundish).

double-log PDF plots such as Figure 5 as a linear distribution type, in agreement with theoretical modeling.[29] A growing body of observations from liquid steel within the ladle[28,30,31] indicates that alumina NMI in liquid steel universally have such power-law, linear appearing PDFs. If the NMI in clogging deposits were simply a sample of the NMI inherent in the steel passing by, this linear size distribution type would be expected to reappear in the clog inclusions. Conversely, if the clog were formed as the result of some form of local reoxidation, e.g., by air ingress creating the clogging inclusions freshly at the location where they are seen, then a lognormal PDF would be expected, as this would be a local net transfer reaction. This constitutes the motivation for our application of particle characterization by PDFs to the clogging deposit. The general types of all the measured PDFs in Figure 5 are lognormal, showing a unequivocal curvature over the size range from 1 to 30 μm. This contrasts strongly to NMI floating in the steel during secondary metallurgy.[27,28,30,31] Figure 5 shows the Reference Line

defined by Reference 25 for such power-law PDFs of the NMI from the secondary steel making for comparison. The observation that the inclusions of clogging deposit from the tundish nozzle generally have lognormally distributed sizes is in agreement with the inclusion measurements of Reference 23 on the same steel.

Further, the visually apparent Coarse and Fine layers have systematic differences in size distributions (Figure 5). In the Coarse layers, there is significant amount of very large objects (> 30 μm), which on inspection tend to be microbubbles, sometimes with attached alumina grains along their surfaces. The Coarse layers also display a higher amount of alumina particles than the Fine layers at sizes > 10 μm. The occurrence of these large complexes (both bubbles and large clusters) is what creates the visible distinction between the two kinds of layers.

Moreover, the Overgrowth layer shows the biggest difference to both the Coarse and Fine layers by having no large clusters above 20 μm at all. Further, it has the highest amount of small inclusions and a lower amount of inclusions in the range from 5 to 20 μm. These characteristics imply that this layer is least affected by possible Ostwald ripening effects which would decrease the fine particle numbers in favor of bigger particles. Thus, the Overgrowth layer seems to be the youngest of the microstructures visible in Figure 4, which is also consistent with its location at the inside of the layered deposit as a whole. The lognormal type of the PDFs observed throughout the layered complex suggests that the inclusions captured there were formed by nucleation and growth, but not subjected to PDF linearization processes, such as collision/breakup in liquid steel. This is shown by comparison to the power-law Reference Line in Figure 5, which represents typical linearized NMI PDF from the steel during secondary metallurgy.[28]

2. Summary

Microscopy of the clogging deposit showing the presence of layering has been introduced in this study in detail. Two distinct types of layers have been found:

– the Fine, which contains densely and homogeneously distributed alumina particles, with few bigger inclusions and no microbubbles
– the Coarse, which is characterized by the higher amount of the bigger inclusions and the presence of microbubbles.

Those findings are illustrated by the PDFs of the measured layers. Additionally the Overgrowth layer, crosscutting the pre-existing layering complex, shows the finest alumina particle population, which is consistent with the microstructural age sequence.

3. *Region 2: template mapping on the layering structure*

The layering structure of region 1 shown in Figure 4 contains only a small fraction of sample 2 (Fig. 3), but the same form of layered clogging microstructure has been found in other parts of the clogging deposit. Because the central part of sample 2 shows the thickest continuous sequence of layers along the nozzle (Figure 6, region 2 in Fig. 3), it has been chosen to measure a complete quantitative profile of the layering microstructure from the sidewall contact to inner clog surface. This profile was quantified using EDS template mapping due to the superior spatial resolution of the SEM compared to optical microscopy, allowing more precise characterization of the particle populations. An overview of the second layering clogging structure in sample 2 is given in Figure 6, together with an outline of the layering visible there. A repeating sequence of Coarse (1, 3, 5, 7) and Fine layers (2, 4, 6, 8) counting from the refractory inwards is present. The EDS template mapping has been performed across the entirety of the layered clogging deposit as it can be seen in Figure 6 (rectangles A, B, C). In template mapping, the area of analysis is viewed frame by frame under the SEM in back-scattered electron (BSE) mode, in which inclusions appear dark and steel bright. The frame is segmented by brightness to define regions of interest (the NMI) and only these

regions are mapped by standard SEM EDS spectral imaging, greatly increasing measurement efficiency. We used a magnification of ×1000 yielding an effective pixel size of 0.245 μm. NMI populations in rectangles A, B, C were morphologically characterized by standard image analysis functions. The EDS net count intensities of Al, Mg, and Ti, integrated by Pathfinder routines, were used as R, G, B channels of multichannel images, and the composition was measured as color in the image analysis. The retention of compositional information as maps has advantages over standard automated-SEM composition measurement per particle as it allows subdivisions of complex particles and morphological operations such as analysis of interphase contact relationships. Population properties could then be measured per phase (location, equivalent circular diameter, circularity/aspect ratio, fiber length, and perimeter-to-area ratio for complex-shaped clusters). To isolate the spread of Ti contents in alumina particles, the occurrence of TiN as an overgrowth phase on some NMI was removed by re-segmenting the original BSE framesets excluding the relatively bright TiN (which also removed the very rare MnS or TiS_x overgrowths). Due to the size of the EDS excitation volume, some Ti signal from TiN can overlap into real alumina particles, where the nitrogen peak served as a marker for removal of such spots.

An exemplary template mapping BSE image is shown in Figure 7 (rectangle A). Rectangle A contains the area directly in contact with the porous nozzle stone, and covers both types of already described layers: the Coarse—layer 1 and the Fine—layer 2 (Figure 6). At the irregular refractory contact there is a bubble filled with loose, granular alumina. At the transition between Coarse and Fine layers (1 and 2), the inclusion number density sharply decreases and is followed by a more massive but still fine-grained NMI microstructure. Particle size distributions were calculated as PDFs separately for each layer. For the Coarse layer 1, the distance of 0.25 to 1 mm from sidewall contact was used, and for the Fine layer 2, the distance of 1.5 to 2 mm (see Figure 7). The basic observational data for this complex are given in Table III. The PDF's for both layers are
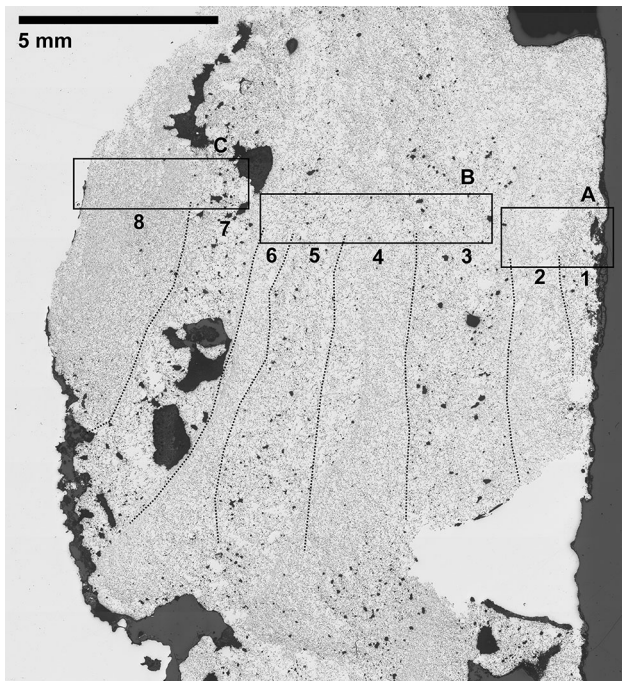

Fig. 6—Enlargement of region 2 of sample 2 shown in Fig. 3 (reflected light optical image). Coarse and Fine layers are outlined in the upper part of the image. Rectangles A, B, and C indicate the areas analyzed by EDS template mapping in detail.
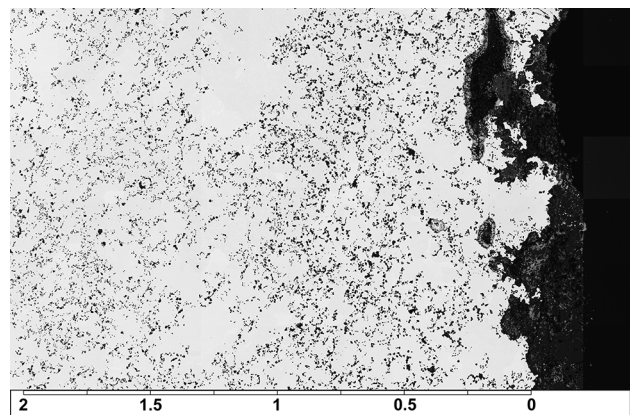

Fig. 7—Rectangle A of the template mapping profile across the clogging deposit (see Fig. 6) Scale bar is in mm at the bottom. The contact to the nozzle is at right.

Table III. Particle Measurement Data for the Template Mapping Transect

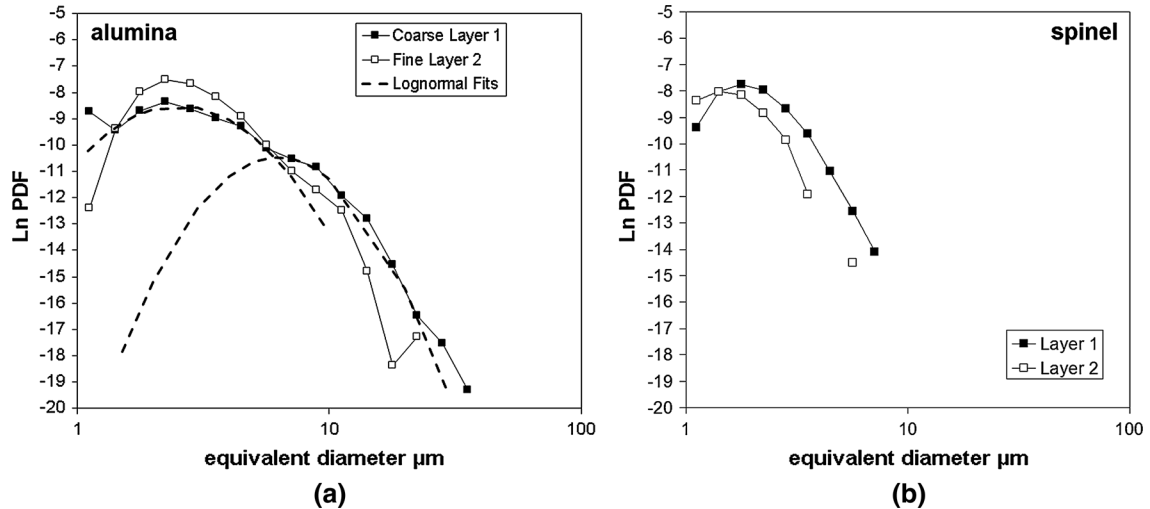| Layers Coarse/Fine	Observation (mm^2)	Number of Aluminas	Number of Spinels	Area fraction Alumina Pct	Area Fraction Spinel Pct
Layer 1 C	1.13	4284	2188	10.2	0.80
Layer 2 F	0.75	3806	719	6.1	0.22
Layer 3 C	2.715	10,640	3067	6.76	0.57
Layer 4 F	1.43	6169	1702	6.69	0.30
Layer 5 C	1.49	6568	2372	7.34	1.00
Layer 6 F	0.63	2798	1204	7.08	0.60
Layer 7 C	0.47	4506	2645	9.43	1.67
Layer 8 F	0.475	5169	2134	9.45	0.95

Fig. 8—Size distributions of NMI particles within the Coarse layer 1 (filled symbols) and the Fine layer 2 (open symbols) of the layering profile (rectangle A). (a) (Left) represents alumina grains, (b) (right) the spinel grains, based on the EDS template mapping segmentation. Dashed lines in the alumina graph are lognormal fits to the data of Coarse layer 1, for the segments from 1.5 to 5 μm (Population I) and from 5 to 20 μm (Population II), respectively, to illustrate the interpretation of the complex PDF shape as a superposition of two lognormal populations.

shown in Figure 8(a). Data below 1 μm equivalent diameter (below 4 × 4 pixels on the image) are discarded as they can be affected by artifacts of the image. Typical error of the PDF curves is ± 0.1 Ln units at Ln PDF = − 8, and ± 0.5 Ln units at Ln PDF = − 17. As spinels were segmented out based on the Mg EDS signal, the same PDF analysis has also been done for the spinels. The resultant PDFs are shown in Figure 8(b).

The data shown in Figure 8 give a more precise view of the morphological differences between the NMI in the Coarse and Fine layers compared to the optical data shown in Figure 5. As it was already broadly concluded previously, all the measured NMI are lognormally distributed in contrast with the power-law size distributions of NMI from the secondary steelmaking.[23,27,28,30,31] Compared to the optically determined PDFs, the SEM-derived data show more complex differences between the two types of layers. As it can be seen, the Coarse layer (1) has a higher frequency of larger alumina particles in the range of 5 to 30 μm, whereas the Fine layer (2) has higher frequencies of small alumina particles in the range ~ 1 to 5 μm.

Moreover, the shape of both distributions appears to be a stack of two separate populations both having the characteristic curvature of lognormals, with a crossover at ~ 5 μm equivalent grain size. The Fine layer shows the visible kink in the distribution at 5 μm indicating that the larger population is still present, but at a lower frequency. The Coarse layer not only has more of the larger particles, but also less fine alumina particles than the Fine layer. We define the apparent subpopulation with grains < 5 μm as Population I, and the other lognormal PDF segment with grains > 5 μm as Population II, both present in all layers. The contrast between the Coarse and Fine layers is also visible in the spinel PDFs: in both layers spinel PDFs are relatively close to ideal lognormals but the Fine layer has significantly smaller spinel grains and less of it. The same treatment has been applied to the NMI data in rectangles B and C (Figure 6). Rectangle B starts in Fine layer 2 and extends up to the Coarse layer 7; rectangle C runs across the innermost edge of the clogging deposit. The results for all the observation areas together are shown in Figure 9; basic observational data are given in Table III.

For alumina, each PDF is based on between 1000 and 10,000 particles; for the less frequent spinel nearly all datasets have over 1000 particles. Figure 9 shows that the lognormal PDF shapes characterize the entire deposit. In detail, however, the PDF curves of Coarse and Fine layer microstructures vary significantly. Population II is consistently higher in the Coarse layers than in the Fine layers. Conversely, Population I is higher in the Fine layers than in the Coarse layers. The innermost layer pair, L7 and L8 stands out by having markedly higher particle frequencies at low sizes than all the previous layers. This is comparable to the character of the Overgrowth layer in the above-described layering complex (region 1 of sample 2, Figure 3, 4 and 5). Close inspection of the lognormals of Population I (2 to 5 μm) in Figures 8 and 9 (layers L1 to L6) shows that the curves are not symmetric lognormals but the small-size

limb is dropping far steeper than the large-size limb. This is the characteristic feature of Ostwald ripening acting on the size distribution, in which large numbers of small inclusions dissolve for only an insignificant rise in the amount of large inclusions, introducing a skewness into the PDF (drop in variance[23,32]). The higher frequencies in the fine grains of L7-L8 (similar to the Overgrowth layer) suggest that these innermost layers have been affected less by Ostwald ripening than the rest of the clogging deposit, and have formed last, which is consistent with its positions on the inner clog surface.

The mineralogical diversity of the Coarse/Fine layer couples can also be shown by tracing specific compositional types of inclusions (see also below, section EDS analysis). Spinel, segmented out on basis of the Mg signal, is shown in the PDF plots above (Figures 8 and 9), but the PDF curves do not show the relative abruptness of the phase makeup variations across the layers. In the EDS template mapping, the locations of the compositionally distinct particles are identified, and thus, number density profiles can be constructed across the layers for each compositionally distinct particle type. Figure 10 (right) shows an example for this. For alumina, it was found that while most alumina grains are chemically pure, a small number of alumina grains have a distinct and well measurable content of Ti of ~ 2 wt pct if measured as TiO_2. These Ti-enriched alumina grains (noted also by References 23 and 33 in clogging deposits of the given type of steel) occur throughout the clogging deposit, and due to the Ti signal they can be segmented out in the template mapping, as shown on the example frame in Figure 10 (left). These grains can still be distinguished from TiN-associated alumina based on the absence of a N signal as described above. Figure 10 shows a number density profile (particles per square mm) using the data of rectangle A, covering layers 1 (Coarse) and 2 (Fine) at the refractory contact. The data show that the Ti-rich alumina fraction closely follows the overall amount of alumina. Irrespective of layer
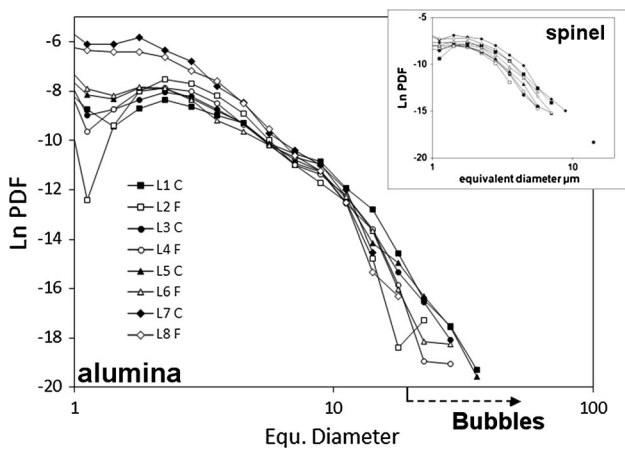

Fig. 9—Layer by layer particle size distributions as PDF curves of rectangles A, B, and C. Black symbols are Coarse layers (L 1, 3, 5, 7); white symbols are Fine layers (L2, 4, 6, 8). L1 is the refractory contact, L8 is the innermost edge of the clogging deposit.
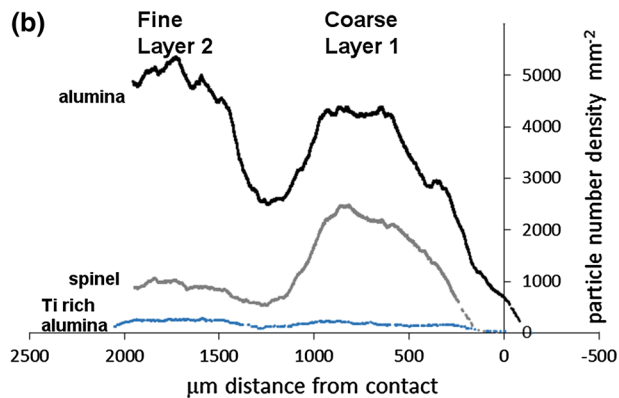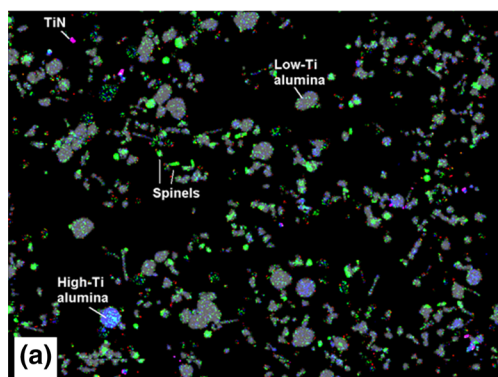

Fig. 10—(a) exemplary frame of the template mapping showing the occurrence of the chemically distinct inclusion types. In this map, Red = N, Blue = Ti, Green = Mg; Al is given as gray background color at half intensity to make the alumina grains visible. The spinel grains are visible as green particles. TiN are visible as red-pink grains from overlapping Ti and N signal. Two compositional varieties of alumina can be distinguished: chemically pure alumina appearing as gray; and Ti-rich alumina with a visible blue color due to minor Ti content (~ 2 wt pct TiO_2 in spot analyses). (b): image shows the phase occurrence of alumina, spinel, and Ti-rich alumina in an example for the contrast between Coarse and Fine layers. The profile shown is the data block of rectangle A, with the refractory contact at right side (refer to Fig. 7 for the refractory border: up to—500 on the horizontal axis). Layers 1 (Coarse) and 2 (Fine) are visible. The number density shown is the number of particle cross-sections per square mm from a moving window of 200 μm across the rectangle width.

type, they constitute ~ 5 pct of all alumina grains. In contrast, the spinel grains are highly enriched in the Coarse layer 1, but much lower in the Fine layer 2: the drop-off is from 34 pct of all particles in Coarse layer 1 to 16 pct of all particles in Fine layer 2 (due to the much smaller size of the spinel grains, this is volumetrically a drop from 7.3 to 3.4 vol pct of the inclusion volume; Table III). Thus, the layers are not only distinct in their overall population densities but also show phase makeup variations from layer to layer (similar variations in spinel have been observed in the other layer pairs, which is not shown).

4. Summary

Within the vertical clogging cross-section in the tundish nozzle of sample 2, a layering microstructure comprising eight distinct layers (alternating Coarse and Fine pairs) has been found. These layers show consistent patterns in their respective size distributions (PDFs). The PDF curves of all the layers show two superimposed populations of particles, each having a lognormal distribution, in contrast to power-law alumina in secondary steelmaking. Application of the superior-resolution SEM template mapping method allowed a precise characterization of the particle PDFs of both types of layers. Population I dominates inclusions from 1 to 5 μm and Population II upwards of 5 μm. The previously described restriction of bubbles to Coarse layers implies that the layering sequence is a repetition of four units, each containing a single Coarse and a single Fine layer. An EDS mapping of inclusions across the whole sequence shows that the layering is also expressed in variable phase fractions, with twice the amount of spinel in the Coarse layers in comparison to the Fine layers. In contrast, the Ti-enriched alumina particles are distributed equally across all layers and make up ~ 5 pct of all alumina grains within the layering microstructure.

5. Minor element analysis of individual alumina grains in the layering structure

To understand the origin of Coarse and Fine layers in the clogging microstructure of sample 2, a detailed SEM EDS analysis of inclusions within the layers of region 1 (Figure 4) was performed. It was found that high-resolution analysis of individual particles resulted in observations which have direct implications for the origins of the layering microstructure. The majority of observed particles have a regular composition (pure Al_2O_3) and familiar shapes: spherical, plate-like, clustered, similar to the classification of Reference 34. An exemplary, regular alumina observed in the layering microstructure can be seen in Figure 11(a)). A significant part of inclusions, however, showed an irregular appearance characterized by metal or complex metal/oxide sub-inclusions encapsulated within the alumina grains. This phenomenon was observed most frequently in particles belonging to the Coarse layers; however, a few of these alumina inclusions with metal sub-inclusions also were found in the Fine layers. Such an irregular Al_2O_3 particle is shown in Figure 11(b). The SEM EDS analyses, performed on encapsulated metal sub-inclusions within particles of the Coarse layers,

show that the compositions of these sub-inclusions contain distinct traces of Cr, V, and Si, which are absent from the steel matrix. A representative EDS spectrum from such a metal sub-inclusion displaying Si, Cr, and V content (in addition to Al and O from the encapsulating particle) can be seen in Figure 11(d)). Another feature characteristic of these complex alumina inclusions is the occurrence of empty voids within their microstructure.

These internally complex alumina particles with metal sub-inclusions appear to form a distinct particle population compared to the Ti-enriched aluminas that are found to be homogeneously distributed throughout the deposit in the EDS template mapping (see above). The Ti-enriched aluminas have cores with enhanced TiO_2 content, making them noticeably brighter in BSE images, and can also have cores with complex inclusion substructure, often in a crystallographically controlled alignment. An example for this is shown in Figure 11(c). These Ti-enriched grains often have very thin outer rims in which the alumina is pure, without detectable Ti. Characteristic for this inclusion variety is the absence of traces of Cr, Si, and V.

SEM EDS chemical analyses of the observed metal sub-inclusions in alumina grains have been done. To increase detection limits for minor and trace elements, we used enhanced acceleration voltage of up to 20 kV and prolonged counting times of up to 300 seconds. In many cases, minor element concentrations in the sub-inclusions were high enough to be accurately measured within 30 to 40 seconds counting times. For the elements Cr, V, and Si this resulted in effective detection limits (signal > 3 σ fluctuation from the background) of 0.025 wt pct Cr, 0.025 wt pct V, and 0.07 wt pct Si (309, 300, and 461, net counts for Cr, V, and Si, respectively—see Figure 12). For Si, this detection limit is largely given by a small amount of Si signal imprinted onto the measurements from the Li-doped Si high-count-rate detectors.

In total, 104 analyses of metal sub-inclusions within alumina particles belonging to the Coarse layers have been performed. Some of the sub-inclusions were smaller than the excitation volume of the electron beam under the chosen conditions. Thus, the raw measurement signal from the sub-inclusions is affected by the relative amount of encapsulating alumina in the excitation volume. To account for this, the intensity of Fe signal from the sub-inclusions was used to indicate the size of the sub-inclusion metal, affecting the intensity of Cr, V, and Si that could be measured from the sub-inclusions. The diagrams in Figure 12 display the net counts of Fe vs Cr, V, and Si measured in the sub-inclusions accordingly, showing all analyses from the Coarse layers. The average 3 σ detection limit has been plotted in Figure 12 as well.

As it can be seen in Figure 12, Cr, V, and Si net counts commonly exceed the 3 σ fluctuation level of the background, and are a real part of the composition of these sub-inclusions. Moreover, as is shown by the arrangement of the measurements on the diagrams, metal sub-inclusions seem to fall into two groups outlining different trends. One group is characterized by elevated Cr, but with relatively low Si net counts, whereas the second group shows the reverse: elevated Si net counts,
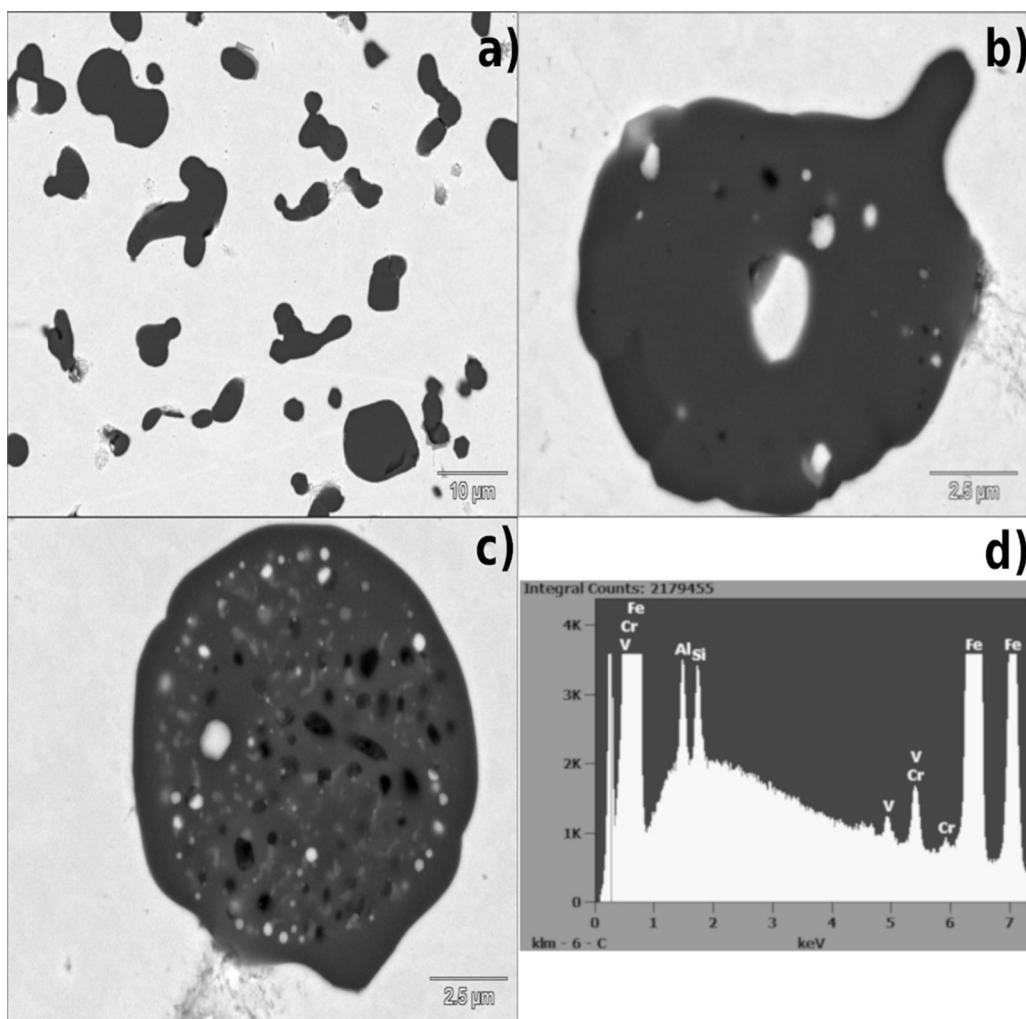
Fig. 11—Exemplary SEM BSE images of (*a*) regular Al_2O_3 particles devoid of substructure and chemically pure; (*b*) Al_2O_3 particle containing metal sub-inclusions with Cr, V, and Si content and voids (black), from a Coarse layer; (*c*) Al_2O_3 particle rich in distinct Ti phases but without traces of Cr, V, and Si; (*d*) EDS spectrum of a metal sub-inclusion in the particle shown in (b), showing explicit Cr, V, and Si peaks.

but relatively low Cr ones. However, the analyses of both trends have been found in the close vicinity of each other. As V is the hardest element to detect, its analyses stay relatively scattered. This feature is displayed when these analyses are plotted as (Cr/Fe) net counts *vs* (Si/Fe) net counts ratios (*i.e.,* as relative concentrations), by two protruding arms enriched purely in Si or purely in Cr separately (Figure 13(a)). Additionally, the analyses of (Cr/Fe) net count ratios observed in the metal sub-inclusions in some of the inclusions in the Fine layers have been plotted, for comparison (Figure 13(b)). The result is that analyses from the Fine layers show only a few compositions with detectable Cr, V, and Si. Quantification of the analyses shows that the average Cr content in sub-inclusions in Coarse layers is 0.14 at. pct, while for Fine layers it is 0.03 at. pct, which is ~ 5 times less.

6. *Summary*

It has been found that the layering microstructure from the tundish nozzle clogging sample 2 is not only visible in the PDFs (Figures 5 and 8), but also can be traced by the microchemical examination of the complex alumina grains within the layers. This is found in the distribution of individual inclusions with metal sub-inclusions enriched in Cr, V, and Si content, which occur nearly exclusively in the Coarse layers.

III. DISCUSSION AND CONCLUSIONS

In the present study, a number of relevant observations of tundish nozzle clogging deposits sampled after casting have been made. The observed microstructures showed the following:

– Solid behavior of the clogging deposit as a unit and its lateral breakup followed by removal during casting (Section II–A);
– Presence of the layering microstructure (Coarse and Fine layers), which implies its depositional character during the casting process (the layers form an age sequence) (Section II–B–1);
– Lognormal size distributions of all of the inclusions found in the tundish nozzle deposit, in contrast to the
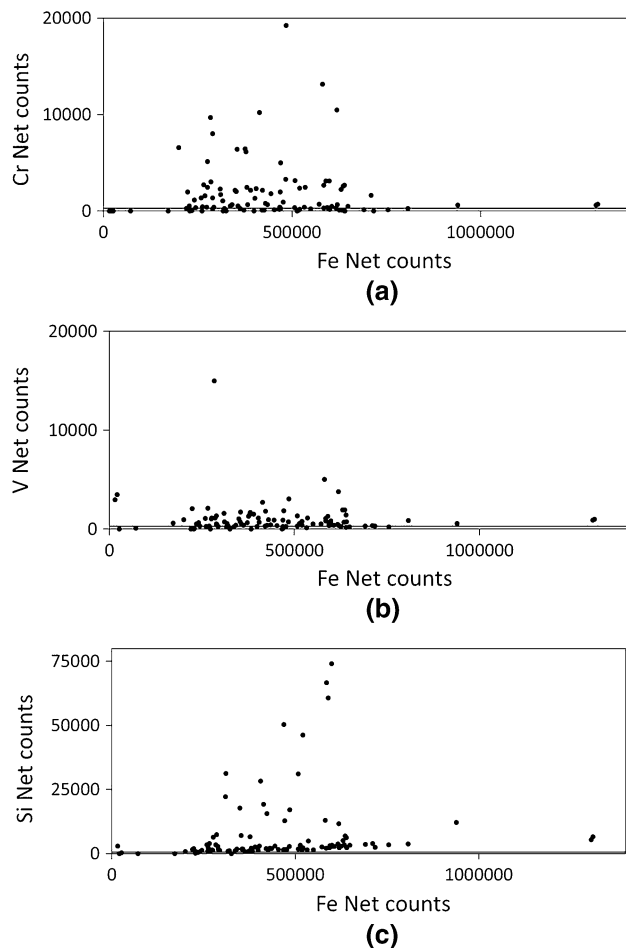
Fig. 12—The scatter plots of the net counts of minor elements present in the metal sub-inclusions in the Coarse layers: (a) Cr vs Fe, (b) V vs Fe, and (c) Si vs Fe, where effective detection limits are displayed (3 sigma levels at 309, 300, and 461, net counts for Cr, V, and Si, respectively).
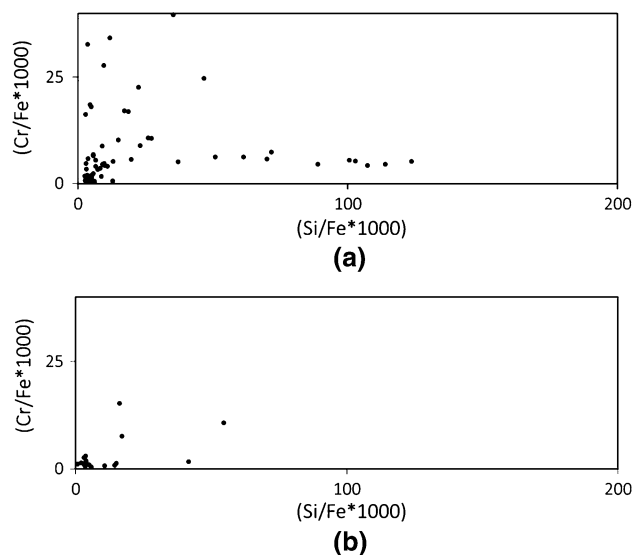

Fig. 13—Comparison of scatter plots of the metal sub-inclusions analyses in two distinct groups of layers: (a) the (Cr/Fe) vs (Si/Fe) net count ratios of the Coarse layers; (b) net counts of (Cr/Fe) vs (Si/Fe) in the Fine layers.

power-law distributions of NMI in the ladle (secondary metallurgy) (Sections II–B–1 and II–B–2)
– Presence of two distinct lognormal particle populations within both Coarse and Fine layers, which can be seen in PDFs: Population I (1 to 5 μm) and Population II (> 5 μm). Moreover, the PDFs of Coarse layers showed more of the Population II than the Fine layers. The two populations require distinct sources for each of them. The layering is not caused by one population gradually changing size (Section II–B–2).
– Spinel occurrence as a second phase in the clogging deposit which is much more concentrated in the Coarse layers, in contrast to the Fine layers (Section II–B–2)
– Repetition of the microstructure after every two layers; Coarse and Fine layers constitute a pair (distinguished by microbubbles, spinel occurrence, and relative abundance of the two alumina populations) (Section II–B–2)
– Alumina particles with distinct Ti content. The Ti appears as ~ 2 wt pct TiO_2 homogeneously distributed in the grain, or combined with distinct Ti-rich phases (TiN, $(Ti,Al)_2O_3$). The Ti-enriched particles occur evenly distributed across the whole deposit without variation between Coarse and Fine layers (Section II–B–2 and II–B–3)
– The Coarse layers almost exclusively contain alumina particles encapsulating metal sub-inclusions. The composition of these sub-inclusions shows significant traces of Cr, V, and Si content. This type of alumina grains is largely absent from the Fine layers (Section II–B–3)

Microstructures such as alumina inclusions embedded in the steel matrix, alumina powder, and microbubbles filled with it have been observed already in 1968[1] and 1974[2] in the same form as observed in this work, and can therefore be assumed to be widespread in the continuous casting of Al-killed steel. Clustering of alumina in liquid steel in the ladle has been analyzed already in 1999[6] and has found recurring attention until today[9,14,35] but not applied to clogging formation understanding. With the significant improvement in the technology used to examine the observed microstructures since the early studies[1,2], it is now possible to directly investigate the formation of observed clogging microstructures (see also Reference 23).

The observations presented in this study provide a new way of looking at the possible formation mechanisms both for the clogging deposit grown in this Ti-alloyed IF steel as well as at the origin of the inclusions found within the clogging microstructures. The most important finding is that all the inclusions in the clog are conforming to lognormal size distributions, in contrast to secondary metallurgy inclusions. Thus, most of the inclusions making up the clog must have formed by new processes of nucleation and growth, which had not yet taken place when the steel was still in the ladle (see Figure 14 for a proposed sketch of the development of the inclusion PDFs).
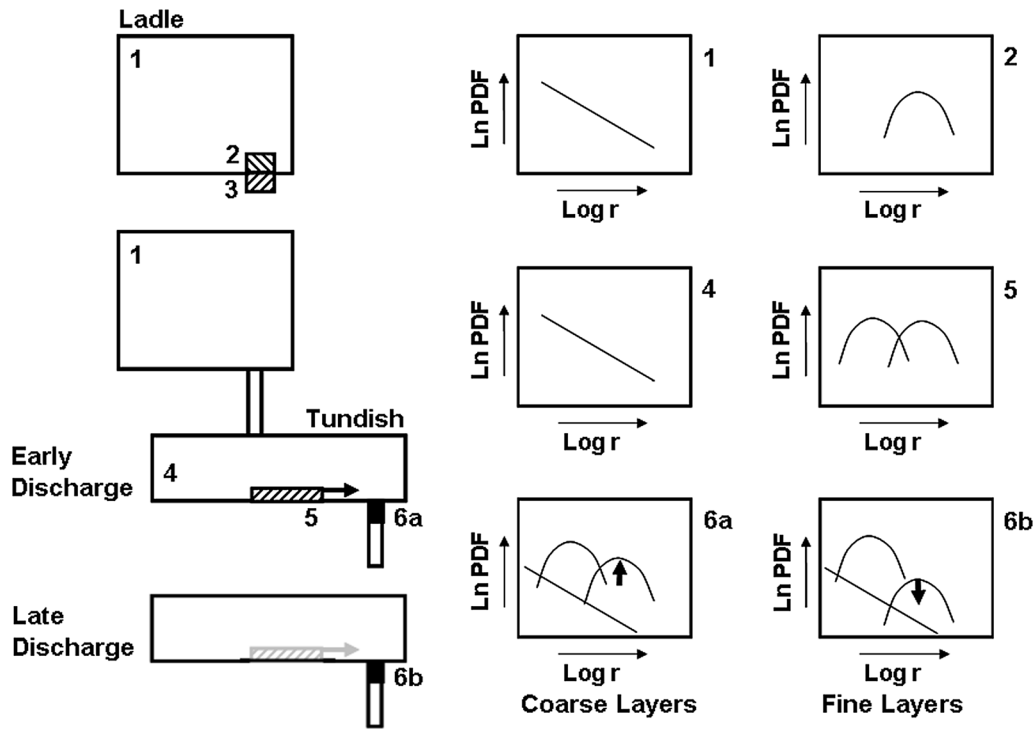
Fig. 14—Sketch of the proposed formation of the inclusion size distributions across the casting installation observed in the clogging deposits. At the left side, a schematic steel-filled ladle is drawn (1), with well filler sand at the bottom (3) and a volume of steel reacting with it (2). Later, the ladle is discharged during casting into the tundish (4) and the remains of zones 2 + 3 are moving over the tundish bottom (5). The clog (6) is growing in the tundish nozzle. The two right-side columns are sketches of the PDF plots of the steel from the different zones (1 to 6). Lognormal Populations I and II are formed in zones 5 and 2 and together build up the clog PDF (6) with a variation from early heat discharge (6a, Coarse layers) to late heat discharge (6b, Fine layers) creating the observed layering contrast.

Further, based on the measured PDFs, we observe that the inclusions can be grouped in two separate lognormal populations: Population I (1 to 5 μm) and Population II (> 5 μm). This finding implies that except the secondary steel making inclusions from the ladle, there must have been at least two distinct origins of the NMI (Figure 14. locations 2 and 5). The presence of secondary metallurgy-derived inclusions has been traced in the occurrence of Ti-enriched inclusions, which are equally distributed throughout the clog. These inclusions represent remnants of the Ti alloying stage in the ladle (Figure 14 location 1).

Clear evidence has been found for the origin of lognormal Population II. It occurs with the highest population density in the Coarse layers, where it is associated with microbubbles, elevated concentrations of Spinel, and alumina clusters with sub-inclusions containing Cr, V, and Si traces. The microchemical characteristics of these inclusions point towards a derivation from the interaction between well filler sand and steel (a chromite-silica sand was used in the cast[24]): During the reaction of the filler sand with the steel[36] coming from the ladle, the liberated oxygen of the sand combines with dissolved A̲l from the steel and forms a new population of alumina grains. Those new grains formed at the reaction interface, where the local steel rich in Cr, V, and Si is captured and encapsulated in them as observed sub-inclusions (it is the only possibility along the liquid route of the steel where Cr, V, and Si

become available together). Simultaneously, the non-reducible part of sand chromite remains behind as spinel, which is entrained into the steel. Both features (metal sub-inclusions and residual spinel) get formed together and are observed to occur together in the Coarse layers of the clog (see Figure 14: inclusions with lognormal characteristics from locations 2 and 5 combine to form the Coarse layers in location 6a).

In contrast, the origin of the Population I particles dominating in the Fine layers is less clear. The lognormal character of this population indicates that it does not come from secondary metallurgy. The absence of specific mineralogical or microchemical characteristics makes it impossible at this point to narrow down their source in the casting process. However, because it must have formed by nucleation and growth, it is likely due to some form of reoxidation of the bulk steel during casting (Figure 14 location 5).

The main finding in the clog is the presence of layering microstructures. The consistent repetition of Coarse and Fine layers there directly proves that the clog as a coherent feature has been built up by depositional processes. Its growth is layer by layer. In fact, the Coarse–Fine layer pairs, with evidence for the well filler sand interaction in every Coarse layer, appear to represent beginning and end of each new ladle cast in the series (Figure 14 loc. 6a, 6b). Each new ladle brings a new batch of well filler sand into the tundish, which is reflected in the formation of a new Coarse layer, with

microbubbles, enhanced spinel amounts, and Cr, Si, and V traces. Coarse and Fine layers make up roughly equal portions of the entire clog volume, which means that about half of the clog grows specifically in the beginning time of each new heat.

Once formed, the observed structures show that the clog behaves as a coherent, semi-solid unit. This is shown by the fractures and detached pieces of the clog material in the three sequential samples (Section II–A). It implies that relatively large blocks of already formed clogging material can be re-entrained into the steel flow and can eventually contaminate the final steel product.

ACKNOWLEDGMENTS

REFERENCES

1. G.C. Duderstadt, R.K. Iyengar, and J.M. Matesa: *J. Met.*, 1968, vol. 20, pp. 89–94.
2. S.N. Singh: *Metall. Trans.*, 1974, vol. 5, pp. 2165–78.
3. K. Rackers and B.G. Thomas: in *78th Steelmaking Conf. Proc.*, 1995, vol. 78, pp. 723–34.
4. K. Sasai and Y. Mizukami: *ISIJ Int.*, 1994, vol. 34, pp. 802–09.
5. K. Sasai and Y. Mizukami: *ISIJ Int.*, 2001, vol. 41, pp. 1331–39.
6. H. Tozawa, Y. Kato, K. Sorimachi, and T. Nakanishi: *ISIJ Int.*, 1999, vol. 39, pp. 426–34.
7. N. Kojola, S. Ekerot, M. Andersson, and P.G. Joensson: *Ironmak. Steelmak.*, 2011, vol. 38, pp. 1–11.
8. W.C. Doo, D.Y. Kim, S.C. Kang, and K.W. Yi: *ISIJ Int.*, 2007, vol. 47, pp. 1070–72.
9. H. Lei and J.C. He: *J. Non-Cryst. Solids*, 2006, vol. 352, pp. 3772–80.
10. O. Araromi, B.G. Thomas, E. Conzemius: *Mat. Sci. Tech. Conf.*, AIST, 2009, pp. 1–10.
11. S. Wu, Y. Wang, L. Zhang, and J. Zhang: *AISTech 2009, Proceedings of the Iron & Steel Technology Conference*, pp. 543–58.
12. M. Long, X. Zuo, L. Zhang, and D. Chen: *ISIJ Int.*, 2010, vol. 50, pp. 712–20.
13. H. Barati, M. Wu, A. Kharicha, and A. Ludwig: *Powder Technol.*, 2018, pp. 29181–98.
14. M. Andersson, J. Appelberg, A. Tilliander, K. Nakajima, H. Shibata, S. Kitamura, L. Jonsson, and P. Joensson: *ISIJ Int.*, 2006, vol. 46, pp. 814–23.
15. W. Fix, H. Jacobi, and K. Wuennenberg: *Steel Res.*, 1993, vol. 64, pp. 71–76.
16. Y. Gao and K. Sorimachi: *ISIJ Int.*, 1993, vol. 33, pp. 291–97.
17. T. Matsui, T. Ikemoto, K. Sawano, and I. Sawada: *Taikabutsu Overseas*, 1997, vol. 18, pp. 3–9.
18. S. Basu, S. Choudhary, and N. Girase: *ISIJ Int.*, 2004, vol. 44, pp. 1653–60.
19. J.H. Lee, M.H. Kang, S.K. Kim, and Y.B. Kang: *ISIJ Int.*, 2018, vol. 58, pp. 1257–66.
20. F. Tehovnik, J. Burja, B. Arh, and M. Knap: *Metalurgija*, 2015, vol. 54, pp. 371–74.
21. B. Harcsik, P. Tardy, and G. Karoly: *Rev. Metall.*, 2012, vol. 109, pp. 177–86.
22. M. Burty, L. Peeters, E. Perrin, S. Muenzer, P. Colucci, D. Salvadori, F. Schadow, J.M. Valcarcel, and J. Claes: *Rev. Metall.*, 2005, vol. 102, pp. 745–51.
23. E. Zinngrebe, J. Small, S.R. van der Laan, and A. Westendorp: Unpubl. Res. Submitted to *Met. Mat. Ser. B*, 2018 (under review).
24. B Karnasiewicz: Unpubl. Masters Thesis, Univ of Rzeszow, 2017.
25. M.D. Higgins: *Am. Mineral.*, 2000, vol. 85, pp. 1105–16.
26. M.D. Higgins: *Am. Mineral.*, 2002, vol. 87, pp. 171–75.
27. M.A. van Ende, M. Guo, E. Zinngrebe, B. Blanpain, and I.H. Jung: *ISIJ Int.*, 2013, vol. 53, pp. 1974–82.
28. E. Zinngrebe, C. Van Hoek, H. Visser, A. Westendorp, and I.H. Jung: *ISIJ Int.*, 2012, vol. 52, pp. 52–61.
29. L. Zhang, W. Pluschkell, and B.G. Thomas: *85th Steelmaking Conf.*, 2002, vol. 85, pp. 463–76.
30. O. Adaba, P. Kaushik, R. O'Malley, S. Lekakh, L. Von Richards, E. Mantel, and E. Ellis: Iron Steel Technology, 2017, pp. 38–49.
31. M.D. Seo, J.W. Cho, K.C. Kim, and S.H. Kim: *ISIJ Int.*, 2014, vol. 54, pp. 475–81.
32. B. McCoy: *J. Colloid Interface Sci.*, 2001, vol. 240, pp. 139–49.
33. X. Deng, C. Ji, Y. Cui, Z. Tian, X. Yin, X. Shao, Y. Yang, and A. McLean: *Ironmak. Steelmak.*, 2017, vol. 44, pp. 739–49.
34. R. Dekkers: PhD Thesis, Kath Univ. Leuven, 2002.
35. L. Zheng, A. Malfliet, P. Wollants, B. Blanpain, and M. Guo: *ISIJ Int.*, 2016, vol. 56, pp. 926–35.
36. Z. Deng, B. Glaser, M.A. Bombeck, and D Sichen: *Steel Res. Int.*, 2015, vol. 86, pp. 1–10. https://doi.org/10.1002/srin.201500118.
37. M.A. van Ende, M.X. Guo, E. Zinngrebe, R. Dekkers, J. Proost, B. Blanpain, and P. Wollants: *Ironmak. Steelmak.*, 2009, vol. 36, pp. 201–08.
38. A. Pack, S. Hoernes, M. Goebbels, R. Bross, and A. Buhr: *Eur. J. Mineral.*, 2005, vol. 17, pp. 483–93.